Depth-Sensitive Subsurface Imaging of Polymer Nanocomposites Using Second Harmonic Kelvin Probe Force Microscopy

Octavio Alejandro Castañeda-Uribe,[†] Ronald Reifenberger,[‡] Arvind Raman,[*,§] and Alba Avila[*,†]

[†]Department of Electrical and Electronic Engineering and Centro de Microelectrónica (CMUA), Universidad de los Andes, Bogotá 11001, Colombia and
[‡]Department of Physics and [§]School of Mechanical Engineering, Birck Nanotechnology Center, Purdue University, West Lafayette, Indiana 47907, United States

ABSTRACT We study the depth sensitivity and spatial resolution of subsurface imaging of polymer nanocomposites using second harmonic mapping in Kelvin Probe Force Microscopy (KPFM). This method allows the visualization of the clustering and percolation of buried Single Walled Carbon Nanotubes (SWCNTs) *via* capacitance gradient ($\partial C/\partial z$) maps. We develop a multilayered sample where thin layers of neat Polyimide (PI) (~80 nm per layer) are sequentially spin-coated on well-dispersed SWCNT/Polyimide (PI) nanocomposite films. The multilayer nanocomposite system allows the acquisition of $\partial C/\partial z$ images of three-dimensional percolating networks of SWCNTs at different depths in the same region of the sample. We detect CNTs at a depth of ~430 nm, and notice that the spatial resolution progressively deteriorates with increasing depth of the buried CNTs. Computational trends of $\partial C/\partial z$ *vs* CNT depth correlate the sensitivity and depth resolution with field penetration and spreading, and enable a possible approach to three-dimensional subsurface structure reconstruction. The results open the door to nondestructive, three-dimensional tomography and nanometrology techniques for nanocomposite applications.

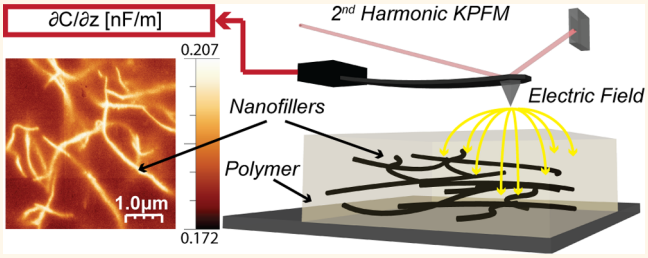

KEYWORDS: AFM · second harmonic · subsurface · depth sensitive · nanocomposites · CNT · polymer

Polymer nanocomposites consisting of nanofillers dispersed in a polymer matrix have emerged as attractive multifunctional materials due to their ability to combine multiple properties such as flexibility, electrical and thermal conductivity, thermo- and photoelectricity, transparency, supercapacitance, and superhydrophobicity in one material.[1−4] Nanofillers such as CNTs,[5−7] graphene,[8−12] alumina nanoparticles,[13−15] silica nanoparticles,[16−18] silver nanowires[19−22] and zinc oxide nanoparticles[23−26] are commonly used in these nanocomposites to tune in the electrical, mechanical, and optical properties. Controlling the physical properties of these multifunctional nanocomposite materials in scaled up manufacturing processes is key to ensure their widespread use in commercial applications. Engineering such nanocomposites materials requires a deep understanding of the links between processing parameters, the multifunctionality, and the nanoscale structure including the size distribution, dispersion, orientation, clustering, and interfaces of the nanofiller inside the polymer matrix. Therefore, there is a great interest in nanoscale-imaging methods that can probe matter beneath the surface to visualize subsurface nanofiller organization.

Second harmonic mapping in Kelvin probe force microscopy (KPFM) has emerged as a key technique for subsurface nanoscale imaging of polymer nanocomposites.[27] This method allows the separation of the surface features in the topography (TP) and surface potential (SP) channels from the subsurface features, which can be observed in the second harmonic channel (capacitance gradient $\partial C/\partial z$ maps).[27−30] As demonstrated in the work by Cadena *et al.*,[27] among the many electrostatic force microscopy techniques for subsurface imaging, nulling the cantilever vibration at the electrical excitation

* Address correspondence to raman@purdue.edu, avila@uniandes.edu.co.

Received for review December 9, 2014 and accepted January 15, 2015.

Published online January 15, 2015
10.1021/nn507019c

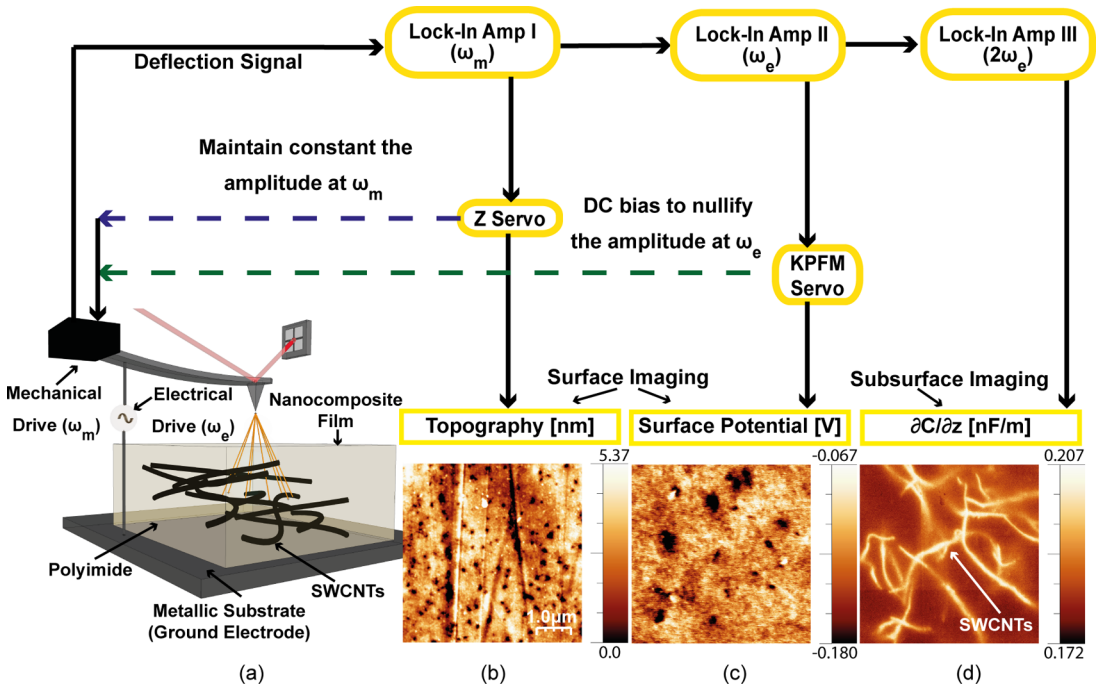

Figure 1. (a) Second harmonic mapping in single-pass KPFM for subsurface imaging of CNT/polymer composites, (b) topography, (c) surface potential, and (d) capacitance gradient ($\partial C/\partial Z$) maps of SWCNT-PI nanocomposites (1 wt %). Image was taken with the following KPFM parameters: $V_{AC} = 3$ V, $\omega_m = 74$ kHz, $\omega_e = 10$ kHz, $A_0/A_{sp} = 0.7$ and a scan size of 5 μm $\times$ 5 μm at a resolution of 1024 by 1024 pixels.

frequency *via* a KPFM servo is essential to ensure that surface charge contrast does not appear in the $\partial C/\partial z$ channel. In Figure 1a, we present a schematic demonstrating the method as implemented in the single-pass mode. In this mode, a conductive cantilever is acoustically excited at a mechanical resonance frequency ω_m and scanned over the sample in the amplitude modulation−AFM (AM−AFM) scheme with a set point oscillation amplitude A_{sp}. Simultaneously, an electric voltage is applied to the cantilever ($V = V_{AC} \sin(\omega_e t) + V_{DC}$) with $\omega_e \ll \omega_m$ while scanning the sample surface. The voltage difference between the cantilever and the sample surface creates an electrostatic force on the cantilever, which generates vibrations in the cantilever at 0, ω_e, and $2\omega_e$ frequencies. The KPFM-servo nulls the amplitude of the cantilever response at the electrical frequency (ω_e) by changing the applied V_{DC}, which is the local SP data. The $\partial C/\partial z$ map, which is known to contain subsurface information,[27−29] is directly obtained from the amplitude of the cantilever response at two times the electrical frequency ($2\omega_e$) (see the Methods for more details). For a heterogeneous sample scanned in the AM−AFM scheme, contrast in the $\partial C/\partial z$ channel is a consequence of the variation in effective local dielectric constants and sample thicknesses.[27]

For the sample developed in this work (SWCNT/PI nanocomposite), the KPFM characterization shows surface information in the TP (Figure 1b) and SP (Figure 1c) maps and subsurface information in the $\partial C/\partial z$ (Figure 1d) maps. The difference in the dielectric constants between the SWCNTs (bright areas) and the PI (dark areas) is reflected in the $\partial C/\partial z$ map, thus enabling the visualization of CNT percolating networks inside the polymer matrix with nanometric resolution.

Despite the remarkable ability of second-harmonic KPFM for subsurface imaging of CNT/polymer nanocomposites, the depth sensitivity and spatial resolution of the method remain poorly understood. Since the electrostatic interaction forces between a composite and a KPFM tip are complex,[31−34] current models have focused on thin[35,36] and thick[37] homogeneous dielectric films. Heterogeneous films have been experimentally studied,[38] but neither models nor measurements have yet provided information regarding depth sensitivity and spatial resolution of second-harmonic KPFM-based subsurface imaging. This challenge is the main motivation for the present work.

In this work, a methodology is presented to determine the sensitivity and resolution of the second harmonic (capacitance gradient $\partial C/\partial z$) KPFM maps in detecting subsurface nanofillers in a polymer matrix. The methodology consists of sequentially KPFM imaging a multilayered PI-coated SWCNT/PI nanocomposite film. We carefully controlled the locations of the subsurface scans within the same region at each PI coating, allowing the subsurface images of the same CNT network to be acquired as a function of the PI film thickness. Additionally, we performed computational simulations of sensitivity and resolution on a probe/nanocomposite configuration, which relate the $\partial C\partial z$ data with the CNTs depth. Based on these computational trends, we developed an algorithm for the

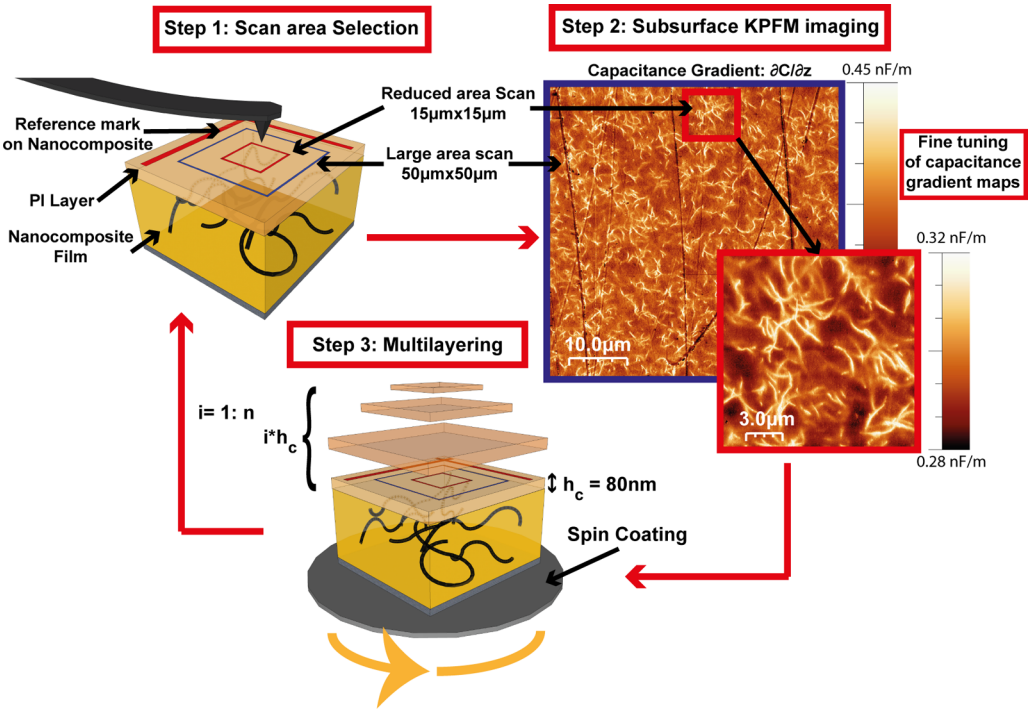

Figure 2. Schematic diagram of the sample multistep preparation and characterization. Step 1: selecting a strategic area. Step 2: acquiiring second harmonic KPFM maps and converting them to capacitance gradient maps. Step 3: coating the nanocomposite sample with a PI film.

three-dimensional reconstruction of the subsurface nanostructure.

The experimental results presented here have been performed in the single-pass approach where mechanical excitation at the cantilever resonance frequency tracks the topography while the electrostatic excitation is at a much lower frequency so as to not interfere with the topography imaging channel. The approach used here can be easily adapted to study the depth limits of other forms of KPFM including two-pass methods and frequency modulation (FM) approaches.

RESULTS AND DISCUSSION

The depth sensitivity and spatial resolution limits of subsurface imaging of nanocomposites were studied using sequentially KPFM imaging of a multilayered PI spin-coated (~80 nm per layer) SWCNT/PI nanocomposite film (Figure 2). A specific CNT network was selected to perform the KPFM measurements as a function of the PI layer thickness (see the Methods for more details).

Figure 3 shows the subsurface KPFM imaging (TP, SP and $\partial C/\partial z$ maps) for four cycles of the multilayering process ($i = 0, 1, 3, 5$). The top row shows that the CNTs cannot be detected in the TP maps and rarely arises in SP maps, thus confirming that the $\partial C/\partial z$ maps (lowest row) indeed provide the best subsurface information on buried CNTs. The presence of subsurface or emergent CNTs can sometimes be also noticed in the SP maps (middle row). Nevertheless, the contrast between the CNTs and the surrounding area is much lower compared with the $\partial C/\partial z$ maps, making it almost imperceptible. This behavior is expected due to the high dependency of the SP channel on the surface properties of the sample, specifically the electronic density, trapped charges, and the chemistry of adsorbed molecules.[39,40] Increased coating thickness decreases contrast between the CNTs and the surrounding media and narrows the range of $\partial C/\partial z$ values over the image (Figure 3 lowest row). These two phenomena indicate a depth limit and a loss of spatial resolution for the CNTs subsurface detection, characterized by a low signal-noise ratio when the $\partial C/\partial z$ range reaches the minimum $\partial C/\partial z$. detectable by the system.

In order to study the depth detection limit a CNT selection mask was used to identify the CNTs closest to the surface in each of the $\partial C/\partial z$ maps of the multilayered sample. The threshold to select the closest CNTs to surface was 96% of the maximum $\partial C/\partial z$ value (red regions in the mask, $(\partial C/\partial z)_{CNT}$), and values below the threshold were considered to be neat PI (blue regions in the mask, $(\partial C/\partial z)_{PI}$), see Figure 4a. The detection limit is defined by the depth at which the difference between $\partial C\partial z$ values ($\Delta C' = (\partial C/\partial z)_{CNT} - (\partial C/\partial z)_{PI}$) reaches the minimum $\partial C/\partial z$ detectable by the system ($(\partial C/\partial z)_{min}$ = 0.8pF/m). From Figure 4b, this detection limit is 400 nm over the depth of the CNT buried in the neat nanocomposite.

The loss of spatial resolution was studied by obtaining the percentage of CNT occupancy in each $\partial C/\partial z$ map at different depths (Figures 5a–d). From these

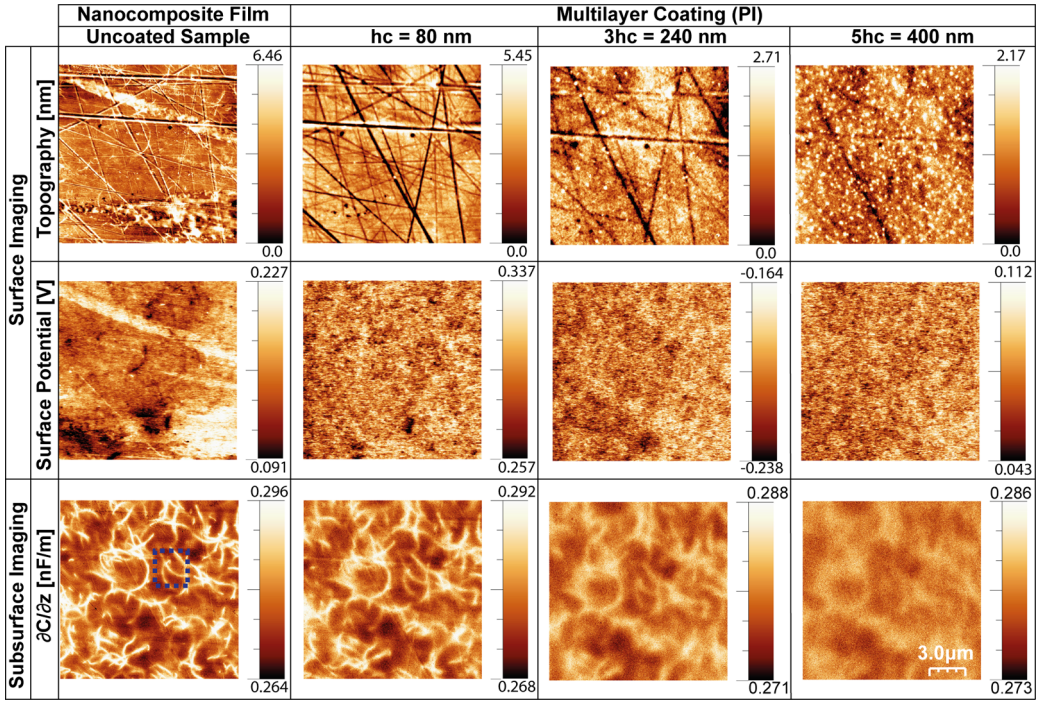

Figure 3. Subsurface KPFM matrix of a multicoated 1 wt % SWCNT/PI composite film. Topography (top row), surface potential (middle row), and $\partial C/\partial z$ (bottom row) for PI multicoatings of 0, 80, 240, and 400 nm thickness. Note that the CNTs are detected as the brightest regions in the subsurface images. The CNT segments depth variations are reflected as intensity changes in the $\partial C/\partial z$ images; see the inset (blue dashed square). The analyzed side of the sample here is the one in contact with the glass slide. The dark lines in the topography images correspond to transfer features from the glass substrate. Images were taken with the following parameters: V_{AC} = 5 V, ω_m = 74 kHz, ω_e = 10 kHz, A_0/A_{sp} = 0.7, scan size of 5 μm × 5 μm and a resolution of 1024 by 1024 pixels.

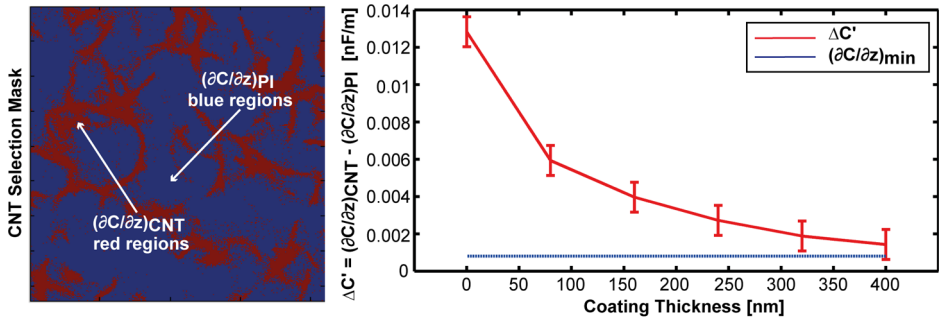

Figure 4. (a) CNTs selection mask of the SWCNT/PI film $\partial C/\partial z$ map. The red regions in the mask represent the highest $\partial C\partial z$ measurements ($(\partial C/\partial z)_{CNT}$), and the blue regions represent the lower ones ($(\partial C/\partial z)_{PI}$). (b) Minimum $\partial C/\partial z$ detectable (blue line) and experimental (red curve) results of the variation of capacitance gradient ($\Delta C' = (\partial C/\partial z)_{CNT} - (\partial C/\partial z)_{PI}$) as a function of the thickness coating. Since the CNTs in the neat nanocomposite film are buried at an initial depth, the curve indicates that the CNTs are distinguishable in this sample at least up to a depth of 400 nm.

maps it can be clearly seen that the spatial resolution for subsurface CNT detection decreases with the increase of PI coatings. For instance, two selected regions (yellow and green squares) in which there is a clear discrimination between CNT and PI disappear at 80 and 160 nm coating thickness because of the increment of the occupancy area of the CNT (spreading of red regions). For the CNT network analyzed in the presented $\partial C/\partial z$ maps, field-spreading leads to 80% apparent CNT coverage with 400 nm thickness coating that contrast the original coverage of 23% in the neat nanocomposite sample (see Figure 5e).

In order to complement the experimental findings concerning the depth sensitivity and loss of spatial resolution, we developed 3D computational simulations of a probe/nanocomposite system using finite elements (see the Methods for details). In the first simulation (depth sensitivity), capacitance gradient calculations of a single CNT buried at different depths (Figure 6a) clearly indicate that CNTs closer to the surface are more easily detected than those buried deeper in the polymer. This can be seen by contrasting parts b and c of Figure 6, where the electric field lines between probe and CNT progressively diminish with

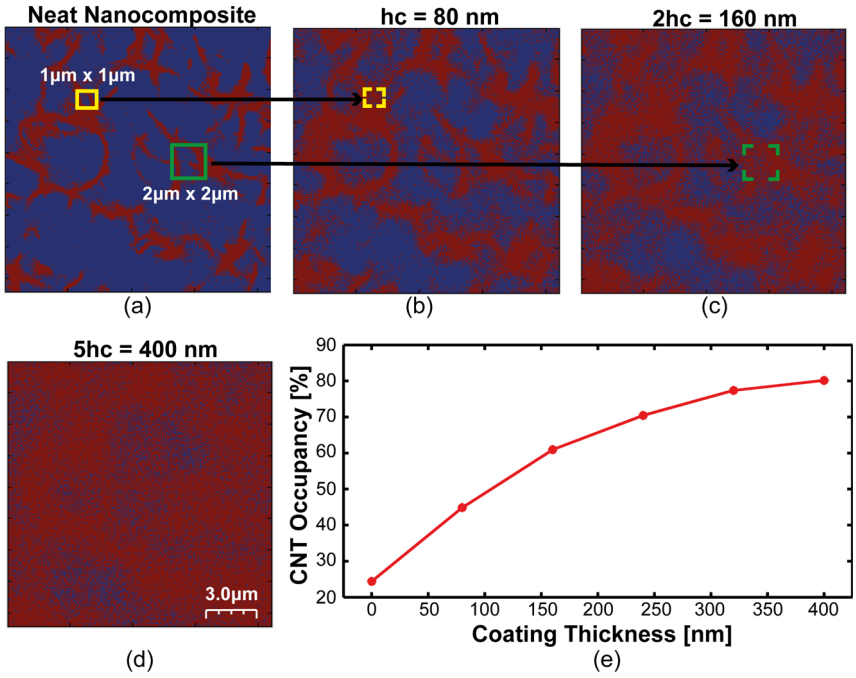

Figure 5. (a) 15 μm $\times$ 15 μm SWCNT/PI film $\partial C/\partial z$ map, (b) 80 nm PI-coated composite film $\partial C/\partial z$ binary map, (c) 160 nm PI-coated composite film $\partial C/\partial z$ binary map, (d) 400 nm PI-coated composite film $\partial C/\partial z$ binary map, (e) CNT occupancy percentage as a function of the thickness coating. At 80% occupancy the CNTs are indistinguishable. Blue regions correspond to $\partial C/\partial z$ values below a threshold (chosen as 96% of maximum $\partial C/\partial z$ value of each map).

the increase of the CNT depth from 5 to 85 nm, respectively. The limit of the depth detection obtained by the computational simulations is extracted from the computed $\Delta C'$ *vs* CNT depth curve (green curve in Figure 6d). The limit was calculated at a 430 nm depth, which is in good agreement with the experimental results in Figure 4. By contrasting with the experimental results it can be deduced that the original depth of the CNT buried in the neat nanocomposite is 30 nm.

For the second simulation (spatial resolution), we used a sample with two CNTs buried in a polymer at the same depths but separated by a fixed distance of 100 nm, see Figure 6e. The effect of field line spreading increases as the CNT are buried farther away from the surface affecting the ability to distinguish two separate CNTs buried at different depths, see Figures 6f,g. In this simulation we systematically calculated the capacitance gradient as a function of the tip scan (tip displacement in the *y* axis) for four different CNT depths: 5 nm, 25, 35, and 85 nm (Figure 6f). The results showed two $\Delta C'$ peaks corresponding to the position of each buried CNT. The height, width and separation of these peaks depend on the CNT depth. With the increase of the CNT depth the height and separation decrease and the width increases until the two peaks are no longer differentiable (Figure 6f, red line). This behavior indicates that the loss of spatial resolution depends not only on the probe geometry[37,41] (cantilever, tip cone and tip apex) but also on the CNT distribution (separation and depth) inside of the polymeric matrix. In particular, CNTs that are located wider apart can be distinguished at greater depths; however, that also results in a noisier $\partial C/\partial z$ signal.

The computational results also suggest a way by which the capacitance gradient data collected in a scan can be used to reconstruct the three-dimensional subsurface CNT network. Using the computational $\Delta C'$ *vs* CNT depth curve to convert experimental observables into CNT depth requires several assumptions. First, the CNTs are conducting, which may not be the case depending on the purity of the CNT sources. Second, each pixel of an embedded CNT is considered to be locally parallel to the surface allowing the use of the computations. Third, the computation does not consider intersection or contacting CNTs. Lastly, the computations use a specific CNT diameter and length, while in reality these dimensions could be different or CNTs might be bundled in the nanocomposite. Notwithstanding these assumptions, it is interesting to consider if these computations can be used to convert the observables into three-dimensional reconstructions.

For this purpose, it is first needed to estimate the depth of the nearest-to-surface CNT in the subsurface image of the uncoated sample, appearing brightest in the capacitance gradient map. With h_{NS} defined as the depth of the nearest-to-surface CNT, h_c defined as the coating thickness and given the $\Delta C'$ calculated from the measurements as a function of the CNTs total depth: $h_{NS} + ih_c$ (were i = 0:5 changes according to the number of coatings.), we adjust h_{NS} until the experimental curve of $\Delta C'$ *vs* total depth $h_{NS} + ih_c$ approximately matches the computational one (Figure 7a, green

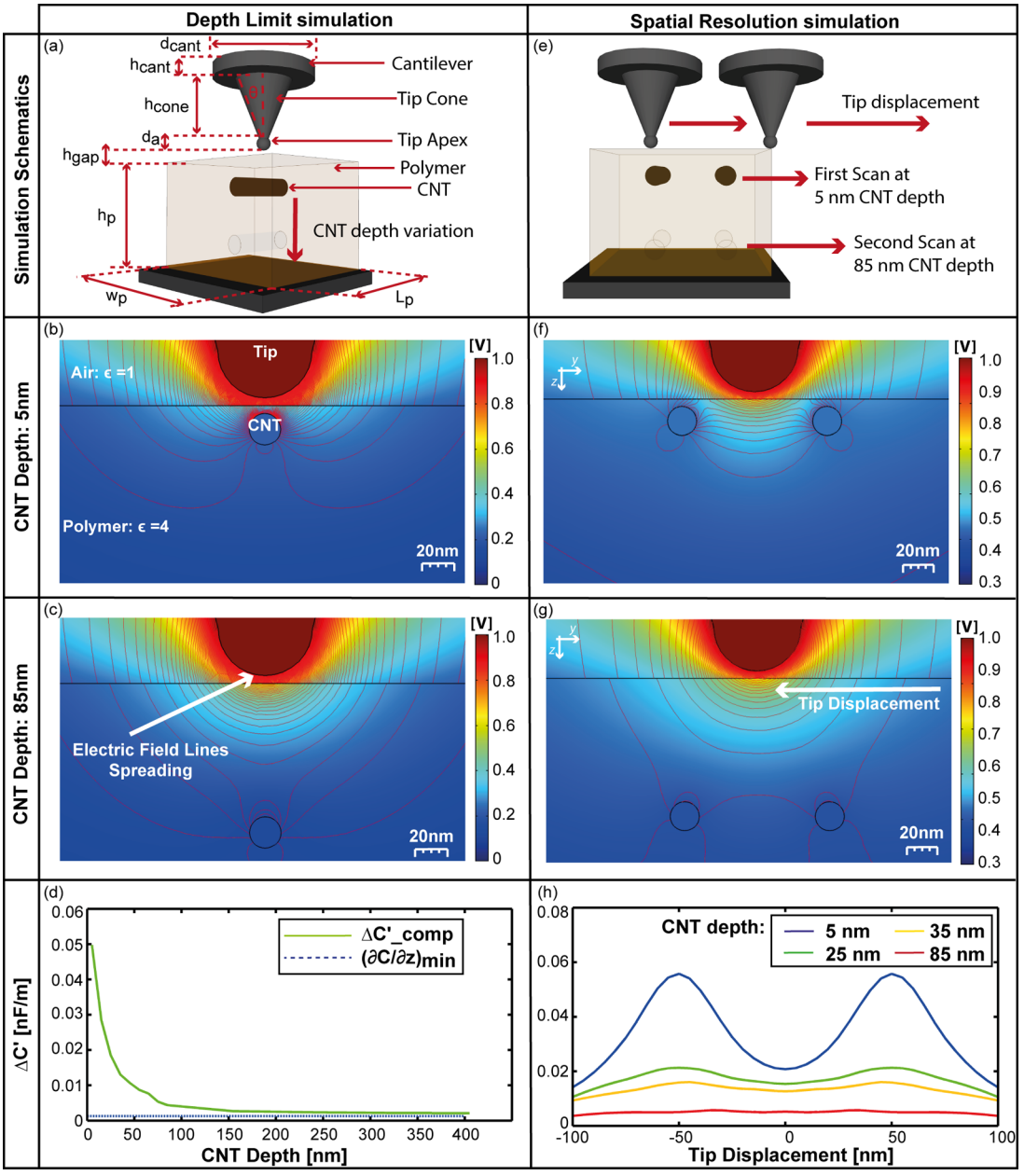

Figure 6. Schematic of depth sensitivity simulation (a). Cross section of the electric potential and electric field lines for a CNT buried at 5 nm (b) and 85 nm (c), respectively. Computational results ($\Delta C'_{comp}$, green curve) of $\Delta C'$ as a function of the thickness coating and minimum $\partial C/\partial z$ detectable (blue dashed line) (d). Schematic of the spatial resolution simulation (e). Cross-section of the electric potential and electric field lines for two CNTs buried at 5 nm (f) and 85 nm (g), respectively. Computational results of $\Delta C'$ as a function of tip displacement for the CNTs buried at 5 nm (blue curve), 25 nm (green curve), 35 nm (yellow curve), and 85 nm (red curve), respectively (h). Simulations were conducted with a tip−sample distance of 10 nm.

and red points). h_{NS} has thus been determined to be ~30 nm. By fitting the $\Delta C'$ *vs* total CNT depth experimental curve (Figure 7 a, red points) to a polynomial form $\Delta C' = A(h_{NS})^{-B}$ (red dashed curve in Figure 7a), we have a master curve that links the experimental $\Delta C'$ at each pixel to the depth of the CNT under the tip. An algorithm that identifies the CNTs on the $\partial C/\partial z$ maps as thin lines and transform each pixel associated with a CNT into a sphere of radius 10 nm with a *z* position (as depth) calculated from the master curve was developed. Using this algorithm, a 3D reconstruction of three selected areas (500 nm x 500 nm) is presented in Figure 7b−d, clearly showing how the depth of the selected CNT networks varies from 10 to 180 nm in the selected areas.

With more advanced computational models, which include CNT orientation and new methods of model validation, this approach may be refined to enable accurate three-dimensional topography of subsurface nanostructure in these composites. Models could be complemented with more information on the fillers associated with their orientation, dispersion, depth,

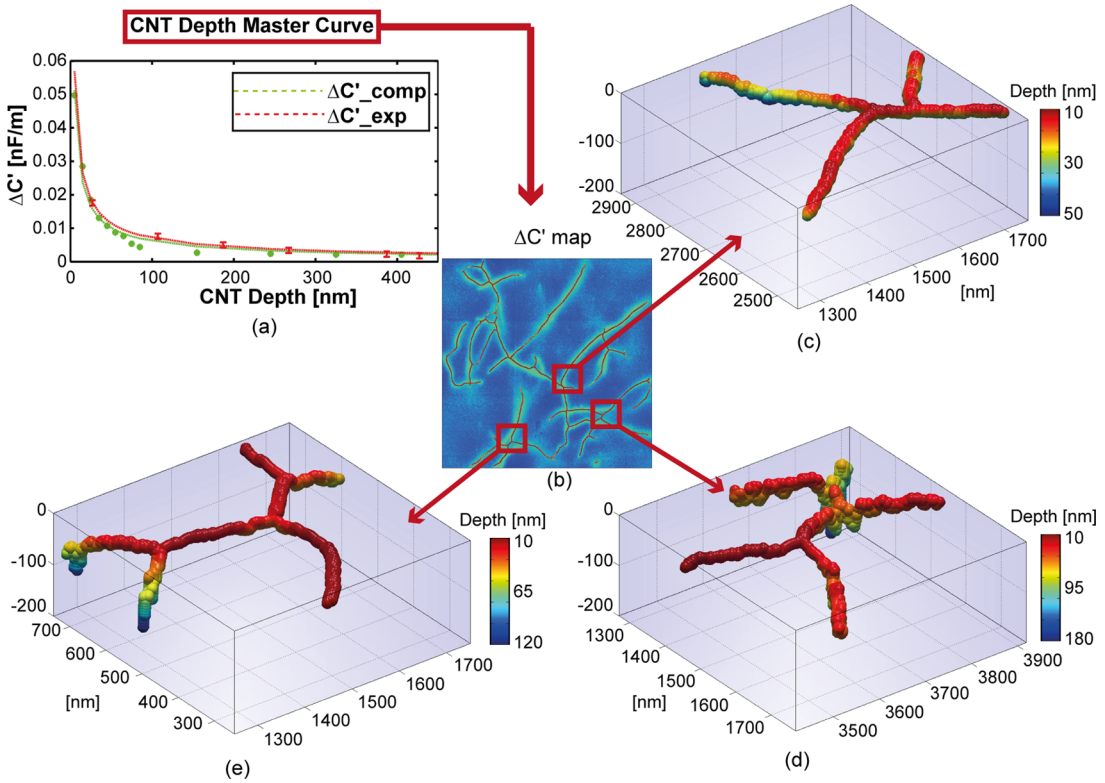

Figure 7. Experimental ($\Delta C'$_exp, red dashed curve) and computational fittings ($\Delta C'_{comp}$, green dashed curve) of the variation of capacitance gradient ($\Delta C'$) as a function of the thickness coating (a). 5 μm $\times$ 5 μm SWCNT/PI film $\partial C/\partial z$ map (b). 3D reconstruction of a selected region of 500 nm $\times$ 500 nm of the SWCNT/PI $\partial C/\partial z$ map (c, d).

and agglomeration metrics. Samples where the CNTs network and topology could be controlled would allow the refinement of models and the correlation with properties.

CONCLUSIONS

The mechanisms that control the depth sensitivity and spatial resolution of second-harmonic KPFM for the subsurface imaging of nanocomposites were explored. By spin-coating controlled thickness layers of neat polymers on the CNT/Polyimide nanocomposite film, we found that CNTs can be detected up to a 430 nm polymer depth and the spatial resolution decreases with CNT depth. The computational simulations of the tip interacting with buried CNTs confirm that the method preferentially detects CNTs closer to the surface and that field line spreading is responsible for blurring the buried CNT networks in the capacitance gradient image. An approach is proposed to use the computational and experimental results for the three-dimensional reconstruction of the subsurface CNT network. These results open the door to nanoscale three-dimensional tomography and nanometrology of nanocomposite materials using second harmonic mapping in KPFM.

METHODS

CNT/PI Composite Sample Preparation. CNT/PI (1 wt % with respect to the polymer) nanocomposites were synthesized by *in situ* polymerization under sonication.[42] HIPCO single-walled carbon nanotubes (SWCNTs, Unidyme) were predispersed in anhydrous dimethylacetamide (DMAc, Acros Organics) for 15 min with a tip sonicator (Q500 Sonicator, Qsonica). To prevent CNTs agglomeration during the polymerization process, Triton-x100 (Aldrich, 0.1 wt % with respect to the solvent) was used as a surfactant, and the dispersion was placed in a sonicator bath (1800 Bransonic Ultrasonic Bath, Branson). For the polymer synthesis, 4−4-oxydianiline (Acros Organics) and an equimolar amount of 3−3,4−4-benzophenone tetracarboxylic dianhydride (Acros Organics) were added to the SWCNT dispersion. After 3 h of polymerization, the nanocomposite was spin coated (6000 rpm, 60 s) on a gold-coated glass substrate (ground electrode) (25 $\pm$ 2 nm gold on a microscope slide, Corning Glass). Solvent (DMAc) was removed at 80 °C, and the nanocomposite was cured in an isothermal process at 100, 150, 200, and 250 °C, thereby resulting in SWCNT/PI films of 20 $\pm$ 1 μm thickness (Figure 1a).

The analyzed side of the sample shown in all presented images here is the one in contact with the glass slide. This is because the CNTs are usually present in the subsurface on this face on the sample.

Second-Harmonic KPFM for Subsurface Imaging of CNT/Polymer Composites. Single-pass KPFM[39,43] with amplitude modulation at the mechanical excitation frequency was used for subsurface imaging SWCNT/PI composite films (20 $\pm$ 1 μm thickness). The method was implemented on an Agilent 5500 atomic force microscope (AFM) with a MAC III accessory while using a conductive cantilever (PPP-EFM, Nanosensors) with a spring constant (k = 2.73 N/m) and a resonance frequency (ω_0 = 77.24 kHz).

The KPFM technique performs independent measurements of surface topography and electrostatic forces in the noncontact mode by exciting the cantilever electrically and mechanically at the same time. The electrical excitation signal ($V = V_{DC} + V_{AC} \sin(\omega_e t)$) composed of a DC voltage (V_{DC}) and an AC voltage (V_{AC} = 5 V) at a frequency (ω_e = 10 kHz) is applied between the conductive probe and the grounded sample while the cantilever is mechanically driven at a frequency (ω_m = 77.14 kHz) with a set point amplitude ($A_{sp} = 0.7A_0$) and a free oscillation amplitude (A_0 = 10 nm). Note that $2\omega_e \ll \omega_m$ so that the cantilever response to electrostatic forces is completely decoupled from the response to mechanical forces.

This KPFM system obtains topography (TP), surface potential (SP), and gradient of capacitance ($\partial C/\partial z$) maps by using three Lock-in amplifiers (LIA). The first LIA selects the cantilever oscillation at ω_m and feeds this signal to a servo controller (*Z*-servo), which maintains the cantilever/sample distance constant and generates the TP maps. The second LIA selects the cantilever oscillation caused by the first spectral component of the electrostatic force ($F(\omega_e) = \partial C/\partial z(V_{sp} + V_{DC})V_{AC} \sin(\omega_e t)$). The SP maps are obtained from a servo controller (KPFM-servo) that nullifies the $F(\omega_e)$ by changing the V_{DC}, so that $V_{sp} + V_{DC} \approx 0$. Finally the $\partial C/\partial z$ maps are obtained by substituting the amplitude of the second spectral component of the electrostatic force ($F(2\omega_e) = (1/4)(\partial C/\partial z)V_{AC}^2$)) obtained by the third LIA into the theoretical expression for the cantilever deflection amplitude at $2\omega_e$.[27] This leads to the following relationship which links the subsurface observable, namely the cantilever amplitude at the second harmonic of electrical excitation frequency $A(2\omega_e)$ to the capacitance gradient $\partial C/\partial z$ at the average position of the vibrating tip over the sample $A(2\omega_e) = (1/4k)(\partial C/\partial z)V_{AC}^2$ for $2\omega_e \ll \omega_0$.

Fundamental KPFM parameters such as tip−sample voltage (V_{AC} = 5 V), average tip−sample distance ($h_{ts} \cong 5$ nm obtained from the amplitude and phase *vs* distance curves), electrical frequency (ω_e = 10 kHz), scan speed (*S* = 0.5 lines/s), scan size (15 μm × 15 μm), and free/set point amplitude ratio ($A_0/A_{sp} = 0$, 7 with A_0 = 10 nm) were carefully selected to ensure that the microscope operates in the attractive regime of oscillation and obtains the highest contrast of CNT subsurface maps avoiding the topographic crosstalk.

The depth sensitivity and spatial resolution limits of subsurface imaging of nanocomposites were characterized using second-harmonic KPFM by repeating the following three steps. First, an imaging area is selected on the SWCNT/PI sample. Cross marks were patterned with a sharp blade prior to identification of the selected areas. These marks allow for the positioning of the cantilever in the same region after each PI coating. Second, the KPFM SP and $\partial C/\partial z$ maps are acquired. The KPFM imaging parameters are tuned-in. All the measurements were taken with the following parameters: cantilever mechanical frequency (ω_m = 77.14 kHz), free/set point amplitude ratio ($A_0/A_{sp} = 0.7$ with A_0 = 10 nm), cantilever spring constant (k = 2.34 N/m), quality factor (Q = 232), electrical frequency (ω_e = 10 kHz), and amplitude of AC voltage (V_{AC} = 5 V). Large 50 μm × 50 μm areas were scanned to locate subsurface CNT networks. We then focused on smaller selected areas (15 μm × 15 μm) where $\partial C/\partial z$ contrast was more distinguished. This contrast differentiates brighter regions where CNTs are closer to the surface from other fillers buried further underneath and neat polymer darker regions (all images were analyzed using WSxM SPM software[44]). Finally, a thin neat PI layer of 80 ± 5 nm was spin coated at 9000 rpm for 60 s and subsequently cured at 250 °C. The spin-coating thickness in each layer was determined by means of AFM tapping mode topography on the interface between PI layer and glass substrate. The steps are repeatedly performed until the $\partial C/\partial z$ contrast measurement is comparable to the system noise level.

Calculations of the Minimum $\partial C/\partial z$ Detectable of the KPFM System. The minimum $\partial C/\partial z$ detectable depends on the minimum $A(2\omega_e)$ that can be detected. This in turn is limited by the system noise. The dominant noise contributions are thermal noise from thermal fluctuations in the tip/cantilever system (th) and instrumental noise generated in the optical detection system (OBD).

The amplitude deflection of the cantilever caused by the thermal fluctuation can be expressed as $A_{noise} = (4K_BTB/Qk\omega_0)^{1/2}(\omega_0^2/((\omega_0^2 - \omega_d^2)^2 + (\omega_0\omega_d/Q)^2)^{1/2})$[43], where K_B is the Boltzmann constant, Q is the quality factor of the cantilever at the resonance frequency, k is the spring constant, T is the temperature, ω_0 is the resonance frequency, ω_d is the drive frequency, and B is the bandwidth of the measurement system. Since the $\partial C/\partial z$ maps are extracted from the amplitude of the cantilever deflection due to the electrostatic force at $2\omega_e$ using $A(2\omega_e) = (1/4k)(\partial C/\partial z)V_{AC}^2$ for $2\omega_e \ll \omega_0$, the amplitude deflection of the cantilever caused by the thermal fluctuations can be expressed as a function of $\partial C/\partial z$ as $(\partial C/\partial z)_{th} = (8/V_{AC}^2)(K_BTBk/Q\omega_0)^{1/2}$. For typical cantilever parameters used here at room temperature and with V_{AC} = 5 V $(\partial C/\partial z)_{th}$ is estimated to be 0.36 pF/m.

The minimum $\partial C/\partial z$ caused by the optical beam deflection noise is estimated as $(\partial C/\partial z)_{OBD} = 4k\eta_{OBD}(\sqrt{B}/V_{AC}^2)$ where η_{OBD} is assumed as the minimum OBD noise reported for an Agilent system $\eta_{OBD} = 100(\text{fm}/\sqrt{\text{Hz}})$.[43] For typical cantilever parameters used here at room temperature and with V_{AC} = 5 V, $(\partial C/\partial z)_{OBD}$ is estimated to be 0.71pF/m. Then the minimum $\partial C/\partial z$ detectable by the system is the combination of the noise contributions: $(\partial C/\partial z)\text{min} = ((\partial C/\partial z)_{th}^2 + (\partial C/\partial z)_{OBD}^2)^{1/2}$, which is estimated to be 0.8 pF/m.

Computational Studies of Probe−Sample Interaction. The electrostatic probe−sample interaction is computed by solving the Laplace equation for electrostatics in 3D using COMSOL 4.3b. No assumption on axisymmetry of the electric field has been made. The metallic probe consists of the cantilever (modeled as a disk of diameter, d_{cant} = 12 μm and thickness, h_{cant} = 3 μm), the tip cone (modeled as cone of height, h_{cone} = 15 μm and aperture angle, θ = 25°), and tip apex (modeled as a sphere of diameter, d_a = 15 μm). The heterogeneous sample is composed of CNTs (modeled as conducting cylinders of radius R_{CNT} = 10 nm and length L_{CNT} = 0.6 μm) buried in a polymer matrix at varying depths but always parallel to the surface. The total interaction volume of the heterogeneous sample is defined as a cube of height h_p = 15 μm, length L_p = 30 μm, and width w_p = 30 μm with a dielectric constant of ($\varepsilon \approx 4$).[28,46] Constant potential boundary conditions were applied on the probe surface (ΔV = 1 V) and at the bottom of the sample (ground electrode), and insulating conditions were on the lateral and upper sides of the simulation box and floating potential boundaries were on the CNTs. For an accurate solution, the mesh was refined at an area that covers the end of the tip and the CNT. A systematic mesh and domain convergence analysis was performed to ensure that computed capacitance gradient difference ($\Delta C'$) changed by less than 0.52% upon further increase in mesh density.

The force acting on the probe was calculated by integration of the built-in Maxwell-stress-tensor function over the tip surface.[47,48] To analyze the electrostatic tip/sample interaction independently of the applied potential, the force was converted into capacitance gradient variations $\Delta C' = C'_{CNT} - C'_{PI}$, where C'_{CNT} is the capacitance gradient, where the probe is located on top of the buried CNT and C'_{PI} is the capacitance gradient where the probe is located on top of a CNT-free region.

In line with the experiments for the KPFM depth sensitivity and spatial resolution of subsurface imaging, two scenarios were simulated keeping the probe at a constant height of the 5 nm above the sample. In the first simulation (depth sensitivity, Figure 6a), capacitance gradient was estimated as a function of the CNT buried depth, which was adjusted from 5 to 405 nm.

For the second simulation (spatial resolution, Figure 6b), the sample was modified integrating two buried CNTs separated by a distance of 100 nm and the capacitance gradient was estimated as a function of the probe displacement across the sample, which was adjusted to scan a 200 nm distance. CNTs buried at depths of 5 nm, 25 nm, 35 and 85 nm were considered.

Conflict of Interest: The authors declare no competing financial interest.

Acknowledgment. We gratefully acknowledge financial support for this research from the Doctoral scholarship program of the Administrative Department of Science, Technology and Innovation of Colombia (COLCIENCIAS) and the grant CMMI: 1344654, SNN: Large Scale Manufacturing of Low-Cost

Functionalized Carbon Nanomaterials for Energy Storage and Biosensor Applications. All of the authors designed and planned the experiments and assisted with sample design, experimental planning, measurements, and result discussions. All of the authors discussed the results and reviewed the manuscript. All of the authors read and approved the final manuscript. O.A.C.-U. performed nanocomposite synthesis, sample fabrication, characterization, and measurements and wrote the manuscript with help from the coauthors.

REFERENCES AND NOTES

1. Hu, S.; Rajamani, R.; Yu, X. Flexible Solid-State Paper Based Carbon Nanotube Supercapacitor. *Appl. Phys. Lett.* **2012**, *100*, 104103(1)–104103(4).
2. Park, S.; Vosguerichian, M.; Bao, Z. A Review of Fabrication and Applications of Carbon Nanotube Film-Based Flexible Electronics. *Nanoscale* **2013**, *5*, 1727–1752.
3. Peng, C.; Zhang, S.; Jewell, D.; Chen, G. Z. Carbon Nanotube and Conducting Polymer Composites for Supercapacitors. *Prog. Nat. Sci.* **2008**, *18*, 777–788.
4. Seo, M. A.; Yim, J. H.; Ahn, Y. H.; Rotermund, F.; Kim, D. S.; Lee, S.; Lim, H. Terahertz Electromagnetic Interference Shielding Using Single-Walled Carbon Nanotube Flexible Films. *Appl. Phys. Lett.* **2008**, *93*, 231905(1)–231905(3).
5. Bara, A.; Bondar, A.; Svasta, P. Polymer/CNTs Composites for Electronic Packaging. *2006 1st Electron. Syst. Technol. Conf.* **2006**, 334–336.
6. McClory, C.; Chin, S. J.; McNally, T. Polymer/Carbon Nanotube Composites. *Aust. J. Chem.* **2009**, *62*, 762–785.
7. Byrne, M. T.; Gun'ko, Y. K. Recent Advances in Research on Carbon Nanotube-Polymer Composites. *Adv. Mater.* **2010**, *22*, 1672–1688.
8. Huang, X.; Qi, X.; Boey, F.; Zhang, H. Graphene-Based Composites. *Chem. Soc. Rev.* **2012**, *41*, 666–686.
9. Qi, X.; Tan, C.; Wei, J.; Zhang, H. Synthesis of Graphene-Conjugated Polymer Nanocomposites for Electronic Device Applications. *Nanoscale* **2013**, *5*, 1440–1451.
10. Lu, H.; Chen, Z.; Ma, C. Bioinspired Approaches for Optimizing the Strength and Toughness of Graphene-Based Polymer Nanocomposites. *J. Mater. Chem.* **2012**, *22*, 16182–16190.
11. Yang, K.; Feng, L.; Shi, X.; Liu, Z. Nano-Graphene in Biomedicine: Theranostic Applications. *Chem. Soc. Rev.* **2013**, *42*, 530–547.
12. Young, R. J.; Kinloch, I. A.; Gong, L.; Novoselov, K. S. The Mechanics of Graphene Nanocomposites: A Review. *Compos. Sci. Technol.* **2012**, *72*, 1459–1476.
13. Maensiri, S.; Laokul, P.; Klinkaewnarong, J.; Amornkitbamrung, V. Carbon Nanofiber-Reinforced Alumina Nanocomposites: Fabrication and Mechanical Properties. *Mater. Sci. Eng., A* **2007**, *447*, 44–50.
14. Mishra, R.; Mukherjee, A. Processing of High Hardness-High Toughness Alumina Matrix Nanocomposites. *Mater. Sci. Eng., A* **2001**, *301*, 97–101.
15. Nishimura, Y.; Aikawa, K.; Choi, S.-M.; Hashimoto, S.; Iwamoto, Y. Relation between Functional Properties of Alumina-Based Nanocomposites and Locations of Dispersed Particles. *J. Ceram. Soc. Jpn.* **2009**, *117*, 836–841.
16. Zou, H.; Wu, S.; Shen, J. Polymer/silica Nanocomposites: Preparation, Characterization, Properties, and Applications. *Chem. Rev.* **2008**, *108*, 3893–3957.
17. Xiong, X.; Li, Q.; Zhang, X.-C.; Wang, L.; Guo, Z.-X.; Yu, J. Poly(vinylidene Fluoride)/silica Nanocomposite Membranes by Electrospinning. *J. Appl. Polym. Sci.* **2013**, *129*, 1089–1095.
18. Sadeghi, M.; Semsarzadeh, M. A.; Barikani, M.; Pourafshari Chenar, M. Gas Separation Properties of Polyether-Based Polyurethane–silica Nanocomposite Membranes. *J. Membr. Sci.* **2011**, *376*, 188–195.
19. Li, L.; Yu, Z.; Hu, W.; Chang, C.; Chen, Q.; Pei, Q. Efficient Flexible Phosphorescent Polymer Light-Emitting Diodes Based on Silver Nanowire-Polymer Composite Electrode. *Adv. Mater.* **2011**, *23*, 5563–5567.
20. Moreno, I.; Navascues, N.; Arruebo, M.; Irusta, S.; Santamaria, J. Facile Preparation of Transparent and Conductive Polymer Films Based on Silver Nanowire/polycarbonate Nanocomposites. *Nanotechnology* **2013**, *24*, 275603(1)–275603(11).
21. Tamboli, M. S.; Kulkarni, M. V.; Patil, R. H.; Gade, W. N.; Navale, S. C.; Kale, B. B. Nanowires of Silver-Polyaniline Nanocomposite Synthesized *via in Situ* Polymerization and Its Novel Functionality as an Antibacterial Agent. *Colloids Surf. B. Biointerfaces* **2012**, *92*, 35–41.
22. Yun, S.; Niu, X.; Yu, Z.; Hu, W.; Brochu, P.; Pei, Q. Compliant Silver Nanowire-Polymer Composite Electrodes for Bistable Large Strain Actuation. *Adv. Mater.* **2012**, *24*, 1321–1327.
23. Jood, P.; Mehta, R. J.; Zhang, Y.; Peleckis, G.; Wang, X.; Siegel, R. W.; Borca-Tasciuc, T.; Dou, S. X.; Ramanath, G. Al-Doped Zinc Oxide Nanocomposites with Enhanced Thermoelectric Properties. *Nano Lett.* **2011**, *11*, 4337–4342.
24. De Rancourt, Y.; Couturaud, B.; Mas, A.; Robin, J. J. Synthesis of Antibacterial Surfaces by Plasma Grafting of Zinc Oxide Based Nanocomposites onto Polypropylene. *J. Colloid Interface Sci.* **2013**, *402*, 320–326.
25. Rodríguez-Tobías, H.; Morales, G.; Rodríguez-Fernández, O.; Acuña, P. Effect of Zinc Oxide Nanoparticles Concentration on the Mechanical Properties and UV Protection of *In Situ* Synthesized ABS Based Nanocomposites. *Macromol. Symp.* **2013**, *325–326*, 147–155.
26. Zhao, H.; Li, R. K. Y. A Study on the Photo-Degradation of Zinc Oxide (ZnO) Filled Polypropylene Nanocomposites. *Polymer* **2006**, *47*, 3207–3217.
27. Cadena, M. J.; Misiego, R.; Smith, K. C.; Avila, A.; Pipes, B.; Reifenberger, R.; Raman, A. Sub-Surface Imaging of Carbon Nanotube-Polymer Composites Using Dynamic AFM Methods. *Nanotechnology* **2013**, *24*, 135706(1)–135706(13).
28. Zhao, M.; Gu, X.; Lowther, S. E.; Park, C.; Jean, Y. C.; Nguyen, T. Subsurface Characterization of Carbon Nanotubes in Polymer Composites *via* Quantitative Electric Force Microscopy. *Nanotechnology* **2010**, *21*, 225702(1)–225702(9).
29. Jespersen, T. S.; Nygård, J. Mapping of Individual Carbon Nanotubes in Polymer/nanotube Composites Using Electrostatic Force Microscopy. *Appl. Phys. Lett.* **2007**, *90*, 183108(1)–183108(3).
30. Nonnenmacher, M.; O'Boyle, M. P.; Wickramasinghe, H. K. Kelvin Probe Force Microscopy. *Appl. Phys. Lett.* **1991**, *58*, 2921–2923.
31. Hudlet, S.; Saint Jean, M.; Guthmann, C.; Berger, J. Evaluation of the Capacitive Force between an Atomic Force Microscopy Tip and a Metallic Surface. *Eur. Phys. J. B* **1998**, *2*, 5–10.
32. Sacha, G. M.; Sahagún, E.; Sáenz, J. J. A Method for Calculating Capacitances and Electrostatic Forces in Atomic Force Microscopy. *J. Appl. Phys.* **2007**, *101*, 024310(1)–024310(4).
33. Sacha, G. M.; Sáenz, J. J. Cantilever Effects on Electrostatic Force Gradient Microscopy. *Appl. Phys. Lett.* **2004**, *85*, 2610–2612.
34. Law, B.; Rieutord, F. Electrostatic Forces in Atomic Force Microscopy. *Phys. Rev. B* **2002**, *66*, 035402(1)–035402(6).
35. Fumagalli, L.; Ferrari, G.; Sampietro, M.; Gomila, G. Dielectric-Constant Measurement of Thin Insulating Films at Low Frequency by Nanoscale Capacitance Microscopy. *Appl. Phys. Lett.* **2007**, *91*, 243110(1)–243110(3).
36. Gomila, G.; Toset, J.; Fumagalli, L. Nanoscale Capacitance Microscopy of Thin Dielectric Films. *J. Appl. Phys.* **2008**, *104*, 024315(1)–024315(8).
37. Fumagalli, L.; Gramse, G.; Esteban-Ferrer, D.; Edwards, M. a.; Gomila, G. Quantifying the Dielectric Constant of Thick Insulators Using Electrostatic Force Microscopy. *Appl. Phys. Lett.* **2010**, *96*, 183107(1)–183107(3).
38. Arinero, R.; Riedel, C.; Guasch, C. Numerical Simulations of Electrostatic Interactions between an Atomic Force Microscopy Tip and a Dielectric Sample in Presence of Buried Nano-Particles. *J. Appl. Phys.* **2012**, *112*, 114313(1)–114313(6).
39. Magonov, S.; Alexander, J. Single-Pass Kelvin Force Microscopy and dC/dZ Measurements in the Intermittent Contact: Applications to Polymer Materials. *Beilstein J. Nanotechnol.* **2011**, *2*, 15–27.

40. Jacobs, H. O.; Leuchtmann, P.; Homan, O. J.; Stemmer, A. Resolution and Contrast in Kelvin Probe Force Microscopy. *J. Appl. Phys.* **1998**, *84*, 1168–1173.
41. Gramse, G.; Gomila, G.; Fumagalli, L. Quantifying the Dielectric Constant of Thick Insulators by Electrostatic Force Microscopy: Effects of the Microscopic Parts of the Probe. *Nanotechnology* **2012**, *23*, 205703(1)–205703(7).
42. Misiego, C. R.; Pipes, R. B. Dispersion and Its Relation to Carbon Nanotube Concentration in Polyimide Nanocomposites. *Compos. Sci. Technol.* **2013**, *85*, 43–49.
43. Li, G.; Mao, B.; Lan, F.; Liu, L. Practical Aspects of Single-Pass Scan Kelvin Probe Force Microscopy. *Rev. Sci. Instrum.* **2012**, *83*, 113701(1)–113701(8).
44. Horcas, I.; Fernandez, R.; Gomez-Rodriguez, J. M.; Colchero, J.; Gomez-Herrero, J.; Baro, A. M. WSxM a Software for Scanning Probe Microscopy and a Tool for Nanotechnology. *Rev. Sci. Instrum.* **2007**, *78*, 013705(1)–013705(8).
45. Melcher, J.; Martínez-martín, D.; Jaafar, M.; Gómez-herrero, J.; Raman, A. High-Resolution Dynamic Atomic Force Microscopy in Liquids with Different Feedback Architectures. *Beilstein J. Nanotechnol.* **2013**, *4*, 153–163.
46. Park, C.; Kang, J. H.; Harrison, J. S.; Costen, R. C.; Lowther, S. E. Actuating Single Wall Carbon Nanotube—Polymer Composites: Intrinsic Unimorphs. *Adv. Mater.* **2008**, *20*, 2074–2079.
47. Jackson, J. D. *Classical Electrodynamics*, 3rd ed.; Wiley: New York, 1999; pp 169—194.
48. Griffiths, D. J. *Introduction to Electrodynamics*, 3rd ed.; Prentice Hall: Upper Saddle River, NJ, 1999; pp 351—355.